frontiers | Frontiers in Energy Research

TYPE Original Research
PUBLISHED 19 January 2023
DOI 10.3389/fenrg.2022.1082239

OPEN ACCESS

EDITED BY
Minjie Shi,
Jiangsu University of Science and Technology, China

REVIEWED BY
Yang Shuhua,
University of Jinan, China
Cheng Yang,
Shanghai Institute of Ceramics (CAS), China

*CORRESPONDENCE
Jingwu Zhang,
zjw@ysu.edu.cn

SPECIALTY SECTION
This article was submitted to Electrochemical Energy Conversion and Storage, a section of the journal Frontiers in Energy Research

RECEIVED 28 October 2022
ACCEPTED 30 November 2022
PUBLISHED 19 January 2023

CITATION
Yang M, Zhang J, Wang J, Gao W, Liu D, Li L, Wang Y and Peng Q (2023), Spatial confinement of sliver nanoparticles in nitrogen-doped carbon framework with high catalytic activity and long-term cycling.
Front. Energy Res. 10:1082239.
doi: 10.3389/fenrg.2022.1082239

Spatial confinement of sliver nanoparticles in nitrogen-doped carbon framework with high catalytic activity and long-term cycling

Meng Yang[1], Jingwu Zhang[1]*, Jinming Wang[1], Wei Gao[1], Di Liu[1], Lanjie Li[2], Yimin Wang[3] and Qiuming Peng[1]

[1]State Key Laboratory of Metastable Materials Science and Technology, Yanshan University, Qinhuangdao, China, [2]Chengde Iron and Steel Group Co., Ltd., HBIS Group Co., Ltd., Chengde, Hebei, China, [3]Department of Central Laboratory, The First Hospital of Qinhuangdao, Qinhuangdao, China

The development of efficient, economical and stable oxygen reduction reaction (ORR) electro-catalysts is crucial to energy storage-conversion technology. Reducing metal dimension to nanosize is a promising approach to maximize its efficiency, whereas the migration and aggregation of nanoparticles have severely hampered their large-scale applications. Herein, we report a new catalyst of N-doped carbon-coated Ag nano-particles (Ag NP@N-C), wherein Ag nanoparticles are confined by N-doped carbon framework. This as-synthesized Ag NP@N-C exhibits excellent ORR performance with a half-wave potential of 0.83 V and a limit-current density of 7.03 mA cm^{-2} in an alkaline medium. More importantly, its durability (cycling for 3600 min), methanol resistance ability in alkaline solutions and catalytic properties in rechargeable zinc-air battery outperform those of commercial Pt/C catalyst and other similar Ag-based catalysts reported so far. The main reason stems from the fact that the interaction between Ag nanoparticles and the support of N-doped carbon can be enhanced by the co-work of pyridine nitrogen and carbon vacancy, rationalizing uniform dispersion of Ag particles. Taking into account its simplicity and high electrochemical properties, we believe that spatial confinement might take an effective trajectory to develop new and large-scale catalysts.

KEYWORDS

ZIF-derived catalysts, Ag nanoparticle, oxygen reduction reaction, Zn-air batteries, DFT caculation

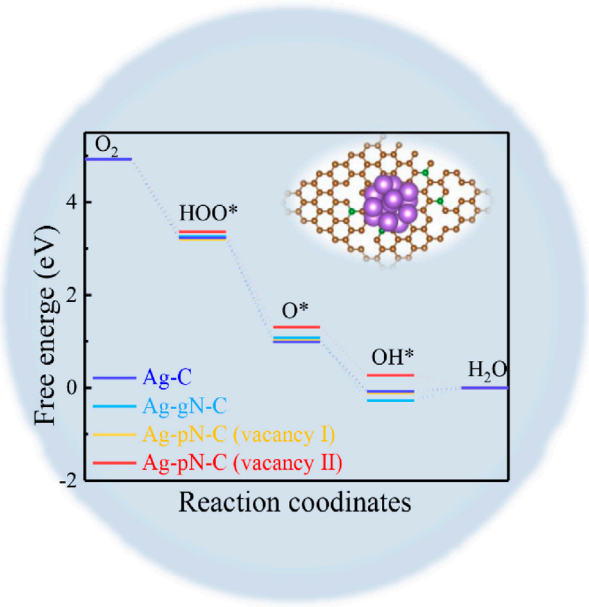

GRAPHICAL ABSTRACT
We prepared a Ag NP@N-C-900 catalyst by a *in-situ* assisted spatial confinement method. This obtained Ag NP@N-C-900 possesses superior ORR performance with a half-wave potential of 0.83 V, excellent stability and methanol resistance ability. Attractively, the primary zinc–air battery based on the Ag NP@N-C-900 air-cathode offers a long cycle of 3600 minutes as well as excellent durability. The catalytic activity and stability exceed most of the Ag-based catalysts reported so far, and are completely comparable to commercially available Pt/C. Spatial confinement of sliver nanoparticles in nitrogen-doped carbon framework with high catalytic activity and long-term cycling.

1 Introduction

To solve the increasingly serious problems of environmental degradation and urgent energy depletion, great efforts have been made to develop clean and sustainable energy (Cano et al., 2018; She et al., 2017). Due to low cost, high theoretical energy density and improved safety, rechargeable metal-air batteries are considered to be one of the most promising energy storage strategies (Su et al., 2017). Oxygen reduction reaction (ORR) on the cathode is one of the main factors affecting the performances of metal air batteries and fuel batteries (Amiinu et al., 2017). However, the hysteresis of the cathode ORR rate severely restricts the development of oxygen reduction electrochemical devices (Yang et al., 2016). Nowadays, platinum (Pt)-based metals have become the most advanced electrocatalysts because of their extremely low overpotential (Iwase et al., 2015). Nevertheless, the high cost, limited reserves, poor durability and vulnerability to chemical sensitivity limited its commercial applications. In this regard, the development of earth-rich catalysts to expand their use and increase their commercial efficiency has aroused great enthusiasm. Researchers are working on non-Pt electrocatalysts, including Ag (Guo et al., 2010), Au (El-Deab et al., 2005), Pd (Jiang et al., 2009), Ni (Asazawa et al., 2009), Fe (Han et al., 2019), Fe-Co dual metal single atoms (Guo et al., 2022; Jiang et al., 2022) and metallic oxide (Roche et al., 2007; Li et al., 2018). However, the preparation process of most metal-based catalysts is complex and often requires pickling. The metallic oxide catalysts have poor performance, especially stability, under alkaline environments. Among these, relatively inexpensive and abundant Ag is deemed as an attractive alternative, because of its high activity. Especially, Ag-C catalysts have gained great attention due to their excellent ORR activity in alkaline solutions. Although the supported Ag catalysts have been developed, unstable support is still a bottleneck to their widespread applications. Due to its higher surface energy, Ag nanoparticles are readily prone to aggregate during the preparation and catalysis process, which may lead to reduced catalytic activity and cycle capacity (Liu et al., 2015; Sun et al., 2020). Therefore, it remains technical challenge to controllably prepare Ag nanoparticles with a small size range on a stable carrier so far.

Recently, the zeolitic imidazolate frameworks (ZIFs) have been considered as ideal precursor materials to attain structural carbon-based materials, due to various surface geometries, large specific surface area, abundant pores and N doping. In addition, ZIFs also can encapsulate small guest nanoparticles (NPs) during the reaction processes. For example, Wang et al. (Wang et al., 2018) reported that the organic ligands coordinating with the central metal atoms (M = Fe, Co, Ni) play a significant role in improving catalytic efficiency. Hu et al. (Hu et al., 2020) further employed MOF-assisted spatial confinement strategy to synthesize Ru single atoms riveted with N-doped porous carbon (Ru SAs-NC) as the efficient electrocatalytic material. Thus, ZIF may be a potential platform to synthesize small-sized

and highly dispersed nanoparticles to enhance ORR catalytic performance.

Herein, we propose an *in-situ* assisted spatial confinement and ion substitution strategy as follows: ZIF-8 was produced companying with the reduction of Ag ion, and then the produced Ag nanoparticles were wrapped in ZIF-8, resulting in nano-sized Ag nanoparticles. The product can be denoted as Ag NP@ZIF-8. Subsequently, a N-doped carbon-coated Ag nano-particles (Ag NP@N-C) was obtained by further carbonization. Attractively, the obtained Ag NP@N-C possessed a superior ORR performance with a half-wave potential of 0.83 V, excellent stability (≈82% activity retention after 15,000 s) and methanol resistance ability, compared with commercial Pt/C in 0.1 M KOH. To expand this catalyst for practical applications, we further used Ag NP@N-C to construct primary zinc-air batteries, which demonstrated a long cycle of more than 3600 min and excellent stability, overwhelming those of commercially Pt/C and other Ag-based materials. The mechanisms of high catalytic performances and structural stability were further interpreted in detail in terms of density functional theory (DFT) calculations.

2 Material and methods

2.1 Syntheses of ZIF-8

Typically, methanol (100 ml) with 2-methylimidazole (3.087 g) was added to methanol (100 ml) with $Zn(NO_3)_2{\cdot}6H_2O$ (1.4000 g) and stirred at room temperature for 9 h to obtain the ZIF-8. The produce was washed several times with methanol and absolute ethanol, the precipitate was collected by centrifugation and drying in a blast oven at 80°C for 12 h.

2.2 Syntheses of Ag@ZIF-8

Typically, $Zn(NO_3)_2{\cdot}6H_2O$ (1.4000 g) and $AgNO_3$ (0.2535 g) were dissolved in methanol (100 ml), then methanol (50 ml) with 2-methylimidazole (3.087 g), methanol (50 ml) with $NaBH_4$ (0.056745 g) and methanol (20 ml) with PVP (0.1000 g) were simultaneously added to the above solution. The mixture was stirred at room temperature for 6 h to obtain the Ag@ZIF-8. The produce was washed several times with methanol and absolute ethanol, the precipitate was collected by centrifugation and drying in a blast oven at 80°C for 12 h.

2.3 Syntheses of Ag NP@N-C-800, Ag NP@N-C-900 and Ag NP@N-C-1000

The Ag@ZIF-8 were pyrolyzed in a tube furnace at 800°C and 900 °C for 2 h around argon atmosphere, respectively. The produce was denoted as Ag NP@N-C-800, Ag NP@N-C-900 and Ag NP@N-C-1000.

2.4 Material characterization

The crystal structure of the sample is detected by XRD (Rigaku D/MAX-2005/PC) using Cu Kα radiation (λ = 1.5406 Å) from 5 to 80° with a scan rate of 4° min-1. The microstructure of the sample was obtained by Scanning electron microscopy (SEM) with a Hitachi S-4800 and FEI Helios G4CX using an accelerating voltage of 20 V–30 kV. TEM and HRTEM images were observed on a Titan ETEM G2 at 300 kV. XPS obtained binding energy and valence on a ThermoFisher X-ray photoelectron spectrometer with Al Kα (1486.71 eV) X-ray radiation (15 kV and 10 mA). The surface areas and pore size distribution was performed on a Micrometrics ASAP2020 analyzer at −196°C (77 K).

2.5 Electrochemical measurements

The electrochemical tests were carried out on a potentiostat/frequency response analysis system (Bio-logic, VSP) at room temperature. The ORR activity was conducted by a rotating disk electrode (RDE, ALS) equipped with a standard three-electrode system. A glassy carbon (GC) disk with the area of 0.07065 cm^2, a Pt mesh and Ag/AgCl (3.5 M KCl) as a work electrode, a counter electrode and a reference electrode, respectively. All potentials were given *versus* RHE ($E_{(RHE)}$ = E(Ag/AgCl)+ 0.969) (Supplementary Figure S1, Supporting Information). In this work, catalyst inks were prepared as follows: 4 mg sample, 0.8 ml of ultrapure water, 0.2 ml of isopropanol and 10 μL Nafion solution were added to a 5 ml sample tube for ultrasonically dispersing 30 min. Then 2 μL of the well-dispersed catalyst ink was dropped onto the glassy carbon electrode and repeated three times. The electrolyte (0.1 M KOH aqueous solution) was bubbled with pure Ar or O_2 for at least 30 min until the solution was saturated before the ORR tests.

2.6 Zinc-air battery tests

The characterization of ORR performance of catalysts by a self-made reversible zinc air battery. The photo of the self-made reversible Zn-air battery is shown in Supplementary Figure S2. Briefly, a polished zinc plate was used as anode, 6.0 M KOH solution was used as electrolyte and a 1 cm × 1 cm foam nickel coated with catalysts ink was used as air cathode. The air cathode was prepared by placing 3 mg sample, 5 mg acetylene black,

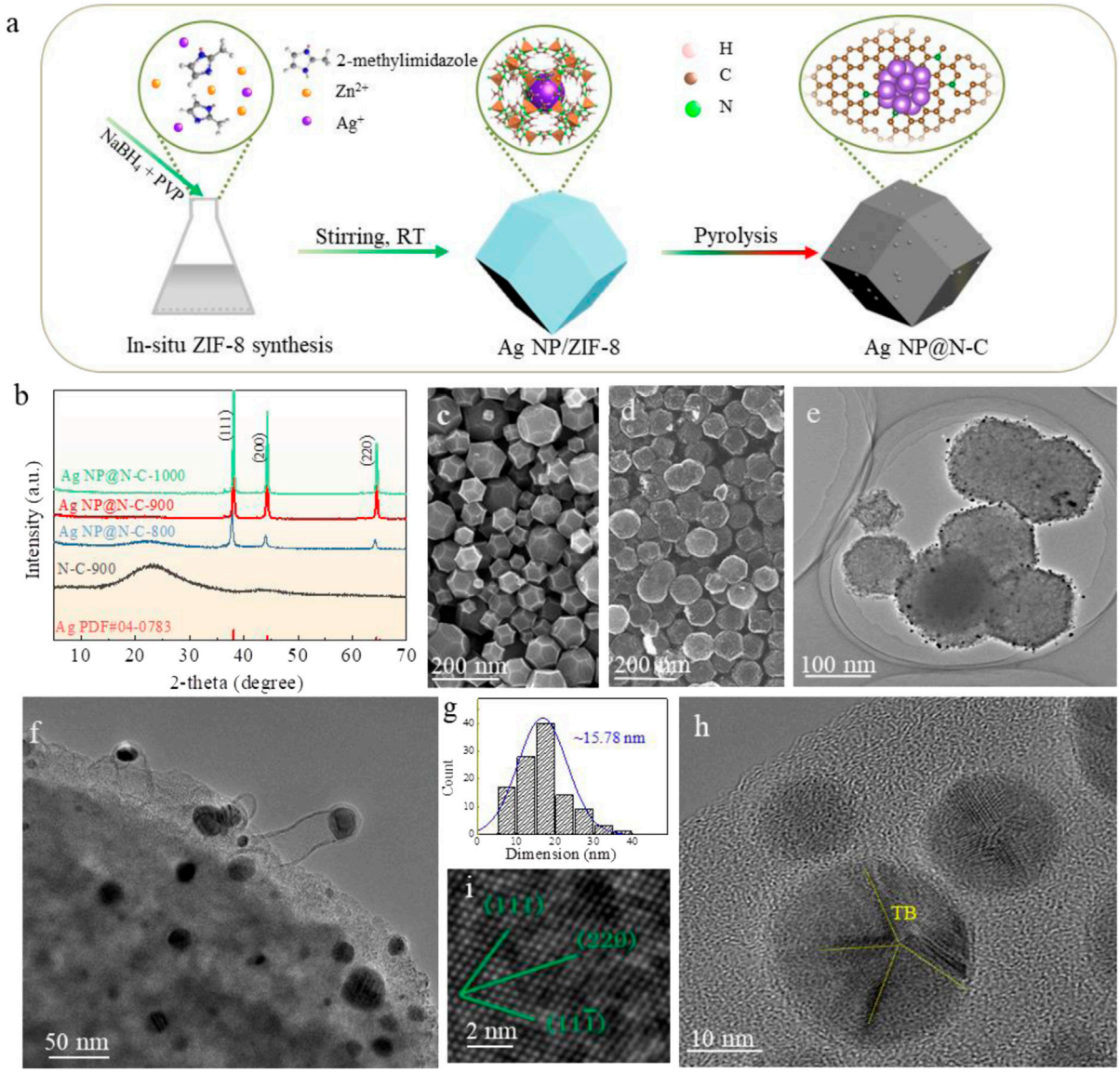

FIGURE 1
Microstructure characterizatics. **(A)** Schematic of the synthesis procedure of Ag NP@N-C, **(B)** XRD patterns of representative N-C-900, Ag NP@N-C-800, Ag NP@N-C-900 and Ag NP@N-C-1000. **(C,D)** Typical SEM image of the ZIF-8 **(C)** and Ag NP@N-C-900 **(D)**. **(E–H)** Typical TEM image of the Ag NP@N-C-900 sample. TEM image of the Ag NP@N-C-900 sample **(E,F)**. High-magnification TEM image **(I)**, **(G)** the particle size distribution of Ag, **(H)** nano twin boundaries in silver particles.

100 mg PTFE emulsion and a small amount of absolute ethanol in a beaker, heated in a 60°C water bath, and the product was coated on foamed nickel and drying at 60°C for 12 h. A nickel strip of 5 cm × 2 mm was taken, and the foamed nickel, the waterproof gas permeable membrane and the nickel strip were pressed together by a tableting machine so that the three did not fall. The galvanostatic charge-discharge tests were performed on a zinc air battery measurement system (Land CT2001A) with a current density of 10 mA cm^{-2} at room temperature.

2.7 Computational details

The density functional theory (DFT) are carried out by VASP code (Kresse and Furthmüller, 1996a). A generalized gradient approximation (GGA) using Perdew-Burke-ernzerhof (PBE) (Kresse and Furthmüller, 1996b; Lai et al., 2016) scheme is used to describe the exchange-correlation energy. The core electrons are represented by the projected enhanced wave (PAW) potential. The kinetic energy cutoff above 500 eV and the K point sampling on the heterojunction interface

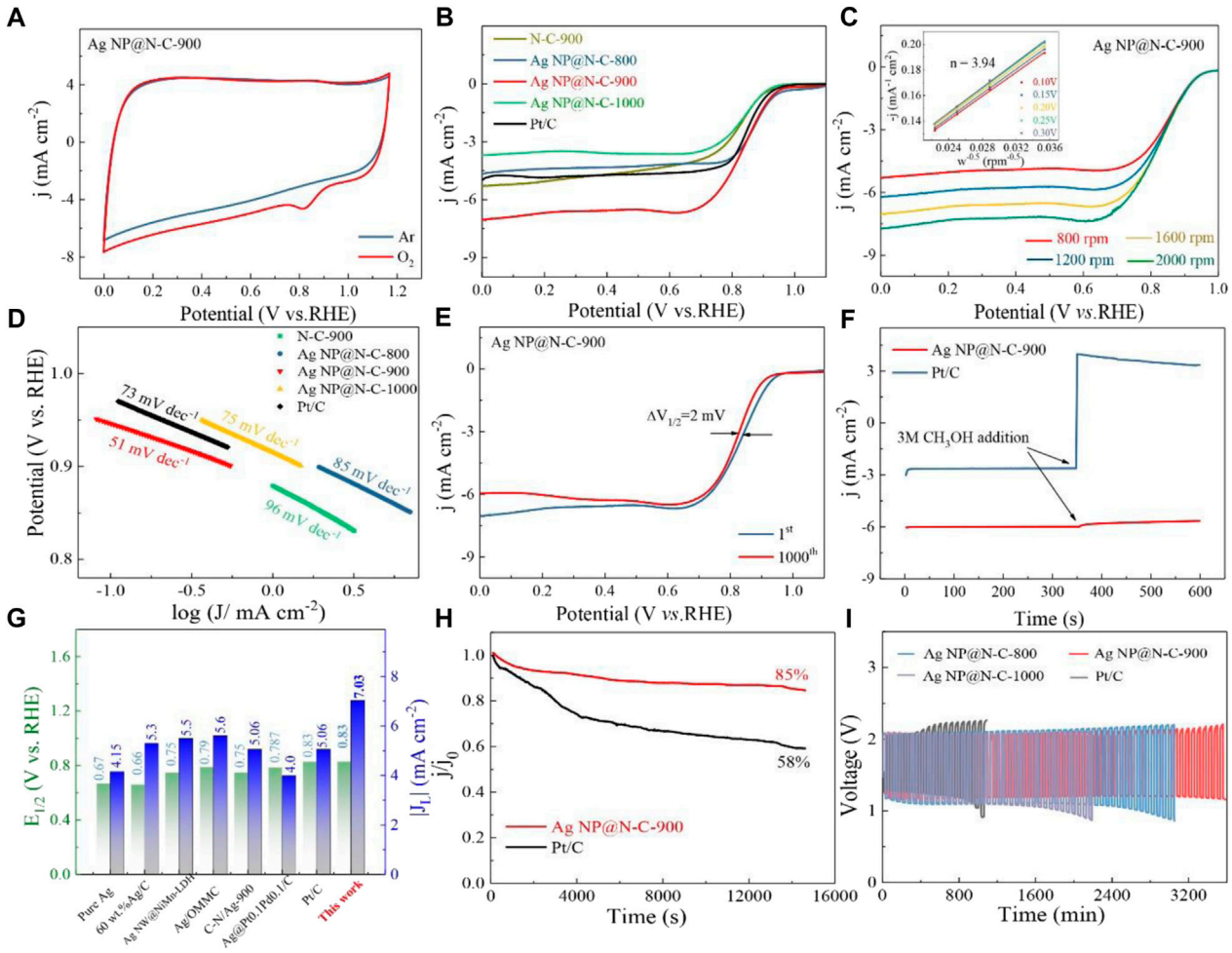

FIGURE 2
Catalytic properties. **(A)** CV curves of the Ag NP@N-C-900 and the commercial Pt/C in a Ar and oxygen-saturated 0.1 M KOH solutions. **(B)** LSV curves of different samples in an oxygen-saturated 0.1 M KOH solutions at the scan rate of 5 mV s^{-1}. **(C)** Polarization curves of the Ag NP@N-C-900 catalyst at different rotating speeds from 800 to 2000 rpm. The inset shows K-L plots at different potentials, **(D)** Tafel slopes of different samples, **(E)** LSV curves at different cycles of the Ag NP@N-C-900 samples in an oxygen-saturated 0.1 m KOH solutions at the scan rate of 5 mV s^{-1}, **(F)** Methanol tolerance test by current–time (*i–t*) curves clock reaction, **(G)** Comparison of ORR performances, **(H)** Electrochemical stability for the Ag NP@N-C-900 and the commercial Pt/C in O_2-saturated 0.1 M KOH electrolyte at 1600 rpm. **(I)** Cycling performances of Zn–air batteries with the different samples as air electrodes.

cell are 5 × 5×1. Structural optimization was performed with a force convergence criterion of 0.01 eV/A and an energy convergence criterion of 10^{-5} eV. A metal cluster containing 13 Ag atoms (Ag13) is used. In the free energy calculation, the step with the smallest change is defined as the potential determining step (PDS) which is the *OH → OH step for the considered catalysts.

3 Results and discussion

3.1 Electrodes characterization

Figure 1A shows the preparation procedure of Ag NP@N-C-X (X = 800, 900, 1000°C) through a simple solution method. Typically, $Zn(NO_3)2{\cdot}6H_2O$ and $AgNO_3$ were dissolved in methanol, then methanol with 2-methylimidazole, $NaBH_4$ and PVP (polyvinyl pyrrolidone) were simultaneously added to the above solution. The mixture was stirred at room temperature for 6 h to obtain the produce (Ag NP@ZIF-8). The Ag NP@ZIF-8 was pyrolyzed in a tube furnace at 800°C, 900°C and 1000°C for 2 h around Ar atmosphere. The products were denoted as Ag NP@N-C-800, Ag NP@N-C-900 and Ag NP@N-C-1000. The samples without Ag nanoparticles were synthesized by a similar method (in the Experimental Section), which were denoted as N-C-800, N-C-900, N-C-1000. Detailed processes can be found in the experimental section.

X-ray diffraction (XRD) patterns of ZIF-8 and Ag NP@ZIF-8 (Supplementary Figure S3, Supporting Information), which

match the pattern of ZIF-8 well, indicating their high crystallinities and similar zeolite-type structures (Lai et al., 2016). It shows the characteristic peaks at (111), (200) and (220) of Ag (JCPDF 04-0783) after polymerization, indicating the loading of Ag nanoparticles (Figure 1B). Figure 1C and Supplementary Figure S4 (Supporting Information) show the typical rhombic dodecahedron morphology of ZIF-8. After pyrolysis at 900°C under Ar atmosphere, the sample is transformed into N-doped porous carbon coated Ag nanoparticle on the surface, and it still maintains the structure of ZIF-8, demonstrating its good thermal stability (Figures 1D, E and Supplementary Figure S5, Supporting Information). In addition, high-magnification TEM image of Ag NP@N-C-900 shows that pyrolysis-generated carbon will coat Ag nanoparticles, which will prevent Ag from agglomerating during pyrolysis and subsequent catalysis (Supplementary Figure S6, Supporting Information). Compared with those of 800°C and 1000°C (Supplementary Figures S7A, B, Supporting Information), the polymerization at 900°C is the best, in which the primitive structure of ZIF-8 is achieved without segregation or collapse. The high-resolution TEM (Figure 1F) image further demonstrates Ag nanoparticles were encapsulated in graphitic carbon shells, with the size of Ag nanoparticles about ~15.78 nm (Figure 1G), also evidenced by FFT image (Figure 1I). The lattice spacing values are found to be 2.26 nm, 1.49 nm and 2.39 nm along to (111), (220) and (11-1), respectively, which are consistent with those of pure Ag facets. Furthermore, Figure 1H also shows the silver nanoparticles are wrapped in the carbon substrate, accompanied by the existence of nanoscale twin boundaries (TB). In addition, according to Raman spectrum, the ratio of peak D to peak G is greater than 1, which proves that there are a large number of defects in carbon (Supplementary Figure S8, Supporting Information).

3.2 Electrochemical evaluation for ORR

To evaluate the effect of annealing temperature on ORR performances, the samples of ZIF-8, carbonized at different temperatures, were primarily investigated on the rotating disk electrode (RDE). The cyclic voltammetry (CV) measurements of the Ag NP@N-C-900 were performed in Ar or O_2-saturated 0.1 M KOH aqueous solutions at a scan rate of 50 mV s^{-1}. Typically, as shown in Figure 2A, in an inert atmosphere saturated with argon gas, the catalyst has no characteristic peak in 0.1 M KOH solution, which proves that the catalyst itself has no side reaction. However, the reduction peak exists in the O_2-saturated environment. The comparison shows that the reason for the existence of the peak is the oxygen reduction reaction, which proves that the catalyst has excellent oxygen reduction catalytic activity. The similar CV curves of the Ag NP@N-C-800 and Ag NP@N-C-1000 are also attained in O_2 and Ar-saturated 0.1 M KOH (Supplementary Figures S9, S10, Supporting Information).

The ORR performances of different catalysts were further investigated by linear sweep voltammetry (LSV). As shown in Figure 2B, the LSV curves showed that the Ag NP@N-C-900 possesses prominent electrocatalytic activity with a half-wave potential ($E_{1/2}$) of 0.83 V, which is equivalent to commercial Pt/C (0.83 V), and a large diffusion-limited current density of 7.03 mA cm^{-2}, which are much better than the commercial Pt/C (5.13 mA cm^{-2}). Compared to other samples at different temperatures, the Ag NP@N-C-900 sample also shows the best ORR performance.

To further study the reaction mechanism of ORR, the RDE measurements of all samples at different speeds (800–2000 rpm) were carried out. The corresponding kinetic parameters and electron transfer number (n) were calculated by Koutecky-Levich (K-L) equation (Zhou et al., 2016). Basically, the J_L value of all electrocatalysts increases with the increasing of rotation rate due to the decrement of diffusion distance (Figure 2C). The inset of Figure 2C illustrates the corresponding K-L plots. Based on the K-L equation, the value of electron transfer number (n) for Ag NP@N-C-900 is calculated to be approximately 3.94, which is close to the theoretical value of 4.0 for Pt/C and better than that of the Ag NP@N-C-800 (n = 3.87) (Supplementary Figure S9B, Supporting Information) and Ag NP@N-C-1000 (n = 3.9) (Supplementary Figure S10B, Supporting Information), indicating that the ORR process mainly includes a one-step four-electron transfer pathway ($O_2 + 2H_2O + 4e^- \rightarrow 4OH^-$)(Bai et al., 2018). The smaller Tafel slope reveals the better ORR activity (51 mV $decade^{-1}$ for the Ag NP@N-C-900 and 73 mV $decade^{-1}$ for the Pt/C, Figure 2D). These results confirm that the catalytic process at the Ag NP@N-C-900 electrode undergoes a four-electron ORR pathway, resulting in a high ORR catalytic efficiency. The stability of Ag NP@N-C-900 is assessed by CV measurements between 0 and 1.2 V at a sweep rate of 50 mV s^{-1} in O_2-saturated 0.1 M KOH. More importantly, after 1000 continuous cycles (Figure 2E), there is a little reduction in $E_{1/2}$ (~2 mV), demonstrating the Ag NP@N-C-900 had the superb stability. Comparison with other samples of the Ag NP@N-C-800 (Supplementary Figure S9C, Supporting Information) and the Ag NP@N-C-1000 (Supplementary Figure S10C, Supporting Information), the Ag NP@N-C-900 still shows better catalytic performance in combination with outstanding structure stability.

In addition, note that an anode fuel (such as methanol) can frequently pass through the polymer membrane from the anode to the cathode, and the cathode catalyst will be poisoned, reducing its catalytic properties (Zhang et al., 2017). Therefore, the Ag NP@N-C-900 and the commercial Pt/C (20 wt%) catalysts were tested for methanol crossover effect via chronoamperometric responses in O_2-saturated 0.1 M KOH electrolyte. The methanol-tolerance results show that

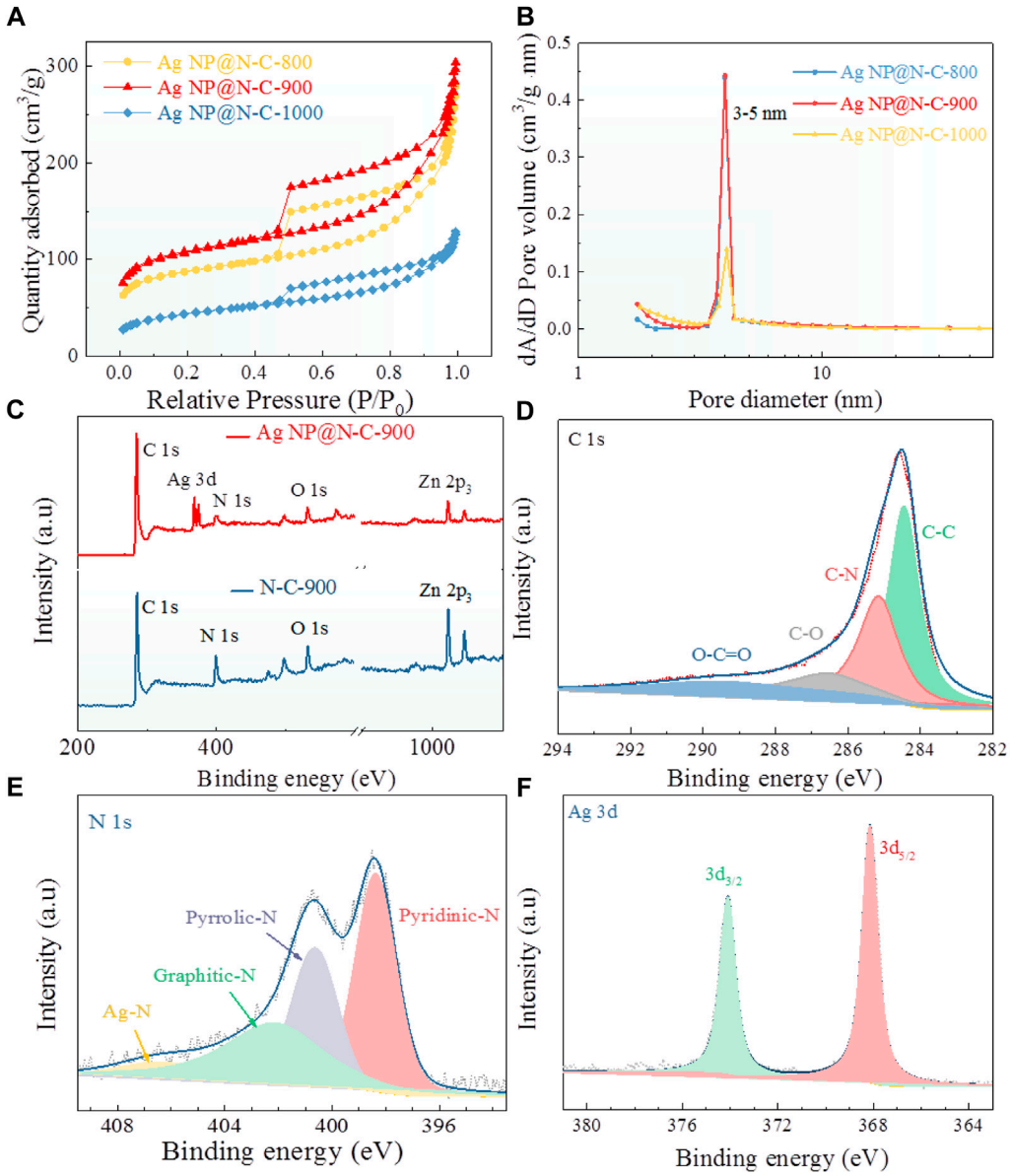

FIGURE 3
Highly catalytic reasons, **(A,B)** N_2 adsorption–desorption isotherms and pore size distribution plots of the Ag NP@N-C-800, Ag NP@N-C-900 and Ag NP@N-C-1000. **(C)** XPS survey spectrum of the N-C-900 (blue), the Ag NP@N-C-800 (red). **(D–F)** XPS profiles of C 1*s* **(D)**, N 1*s* **(E)**, Ag 3*d* **(F)** for the Ag@N-C-900 samples.

there is limited effect on the Ag NP@N-C-900 sample (Figure 2F). On the contrary, when 3 M methanol is injected into the electrochemical cell, the corresponding current density of the 20 wt% Pt/C instantaneously shifts from a cathodic ORR current to a reversed anodic current owing to the methanol oxidation reaction. The current density fluctuation of Pt/C is mainly due to the clogging of the active center on the Pt nanoparticles by the methanol oxidation. More importantly, as summarized in Figure 2G, the performance of the Ag NP@N-C-900 is comparable or even better than many other ORR Ag-based electrocatalysts reported so far (Zhang et al., 2017; Pech et al., 2015; Wu et al., 2017; Dong et al., 2019; Chala et al., 2020).

In addition, as shown in Figure 2H, the Ag NP@N-C-900 exhibits excellent stability (remains more than 82% of its foremost current density) after 16,000 s of continuous operation, which prevails over that of Pt/C (only 58% retention), suggesting that Ag NP@N-C-900 with an outstanding methanol tolerance outperforms the commercial Pt/C. Finally, a series of zinc-air

cells with different samples dispersed nickel foam as air electrode, 6 M KOH electrolyte and zinc plate as an anode was assembled to evaluate the catalytic performance of all the catalysts. As seen in Figure 2I, the battery with the Ag NP@N-C-900 is more stable than the Pt/C counterpart. For the battery with the Ag NP@N-C-900 as the catalyzer, the initial voltage gap during charge–discharge is 0.85 V. After continuous 3600 min operation, the voltage gap only slightly increases 190 mV. Comparatively, the battery with the Pt/C as the catalyzer only cycles for 1300 min, and the voltage gap rises from 0.79 V to 1.87 V. It demonstrates that the zinc–air battery based on the Ag NP@N-C-900 catalyst bestows superior structural stability.

3.3 Catalytic mechanisms

The outstanding electrocatalytic performances and stability of the Ag NP@N-C-900 are mainly related to the well-distributed Ag nanoparticles encapsulated in the carbon layer, hierarchical porous structure and the high concentration of pyridine nitrogen doping.

A carbon layer covered on the surface of Ag nanoparticles prevents their leaching and aggregation during the catalysis process. The hierarchical porous structure of the material is one of the important reasons for high performance of oxygen reduction. It is because the hierarchical porous structure can provide more active sites for oxygen reduction and facilitate electron transport and mass transport. The N_2 adsorption/desorption isotherm was carried out to characterize the surface area and porosity of Ag NP@N-C-X (Figures 3A, B). Differing from the other electrodes, the Ag NP@N-C-900 sample bestows the largest Brunauer–Emmett–Teller (BET) surface area, and then the large specific surface area and porous structure allow for the exposure of active sites and rapid mass transfer kinetics. Moreover, the Ag NP@N-C samples shows typical isotherms with hysteresis loops at high pressure region, generally ascribed to the mesoporous structure (Ramaswamy et al., 2013). The such mesoporous structure can be further verified by the pore size distribution plots (Figure 3B). Furthermore, the doping of carbon materials with N can easily alter the electron neutrality of adjacent carbon atoms to form positively charged sites, which is conducive to O_2 adsorption and reduction (Liu et al., 2017).

To ascertain the surface valence state and element bonding composition of the as-prepared samples N-C-900 and Ag NP@N-C-900, the X-ray photoelectron spectroscopy (XPS) has been performed. As revealed in Figure 3C, the full XPS spectrum of the Ag NP@N-C-900 shows the peaks of C 1s, N 1s, O 1s, Ag and Zn 2p which are different from the N-C-900. The C 1s, N 1s and Ag 3 days spectrum (Figures 3D–F) are further analyzed by deconvolution. The high-resolution C 1s XPS spectrum (Figure 3D) includes four sub-peaks: C-C (284.4 eV), C-N (285.1 eV), C-O (286.5 eV) and O-C=O (289.7 eV) (Shen et al., 2017; Bai et al., 2018). The N 1s XPS spectrum shown in Figure 3E can be fitted by four types of N species: pyridine N (398.2 eV, 38.81%), pyrrolic N (399.9 eV, 19.1%), graphitic N (400.8 eV, 29.1%), and Ag-N (406.6 eV, 12.99%)(Zhou et al., 2017; Huang et al., 2018). It is well known that the catalysts with high pyridine N-based carbon have good oxygen reduction performance because pyridine N increases the initial potential of the catalyst (He et al., 2014). Furthermore, the high-resolution spectra of Ag 3p matched the satellite peaks with Ag $3d_{5/2}$ and Ag $3d_{3/2}$ (Figure 3F) belonged to metallic Ag, suggesting that the Ag^0 existed and matches well with the XRD result (Lopez et al., 2005). In addition, with the increase of temperature (Supplementary Figures S11, S12, Supporting Information), the content of pyridine nitrogen is decreased, and Ag-N disappeared when the temperature reaches 1000°C, partially accounting for the deterioration of performances.

To further elucidate the reaction mechanism during electrochemical catalytic process, the ORR elementary steps have been calculated in terms of density functional theory (DFT). Taking into account the large content of graphite N and pyridine N, four models, i.e., Ag-C, Ag-gN-C, Ag-pN-C (Vacancy I) and Ag-pN-C (Vacancy II) (Supplementary Figure S13, Supporting Information), were constructed to compare distinguish the effects of different types of N and vacancy size. Among them, gN represents the doped form of graphitic nitrogen, pN represents the doped form of pyridine nitrogen. The structure of Ag-N-C the graphite nitrogen is simulated where it mainly contains pyridine nitrogen in Ag-N-C (vacancy I) and Ag-N-C (vacancy II). Among them, vacancy I represents a carbon defect lacking one carbon atom, and vacancy II represents a carbon defect lacking two carbon atoms. The result indicates that the excellent ORR catalytic performance of the Ag NP@N-C can be well-understood by the Ag-pN-C (vacancy II) model, wherein the interaction between the metal and support is strengthened by the cooperative interaction of pyridine nitrogen and carbon vacancy, as demonstrated by the shortest Ag-N distance (2.281 Å) among the models (Supplementary Figure S10, Supporting Information). The enhanced interaction can effectively inhibit the migration of Ag nanoparticles in the carbon surface, in good accordance with the well-dispersion of the Ag nanoparticles observed from the TEM images (Figures 1E, F, Supplementary Figure S14, Supporting Information).

The free-energy change of the reaction pathways and the key reaction intermediates are shown in Figures 4A, B for Ag-pN-C (vacancy II) (Supplementary Figures S15–S17, Supporting Information). Specifically, the initial step of the ORR process is to capture O_2 moleculars. In our calculations, the Ag-C, Ag-gN-C and Ag-pN-C (Vacancy I) are characterized with strong adsorption ability with the $E_{ads}(O_2)$ −1.234 eV, −1.106 eV and −1.122 eV, respectively. However, the binding of O_2 and Ag-pN-C (Vacancy I) is greatly alleviated, whereby the $E_{ads}(O_2)$ is only -0.031 eV (Supplementary Figure S18, Supporting

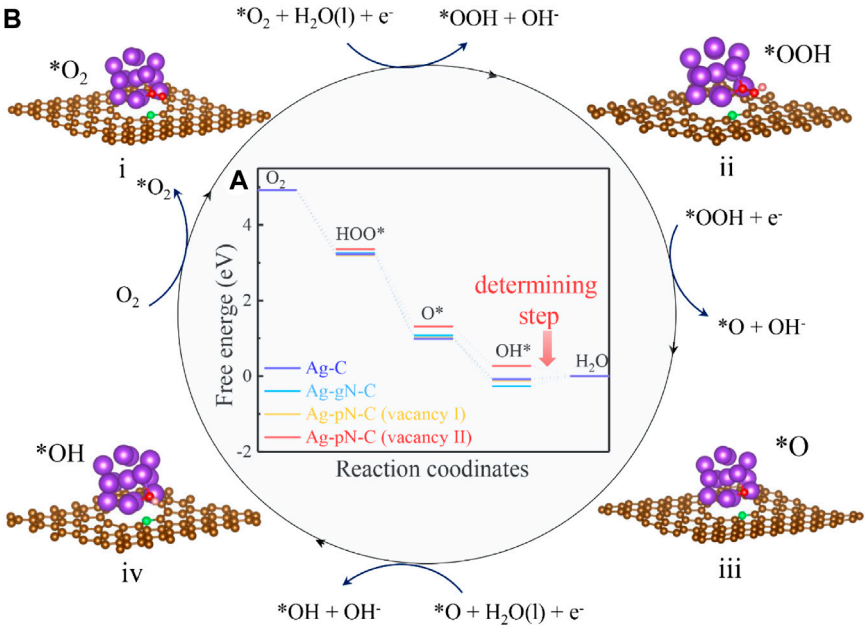

FIGURE 4
DFT calculations **(A)** Free energy diagram of different samples at different optimized adsorbed reaction sites; the oblique lines and corresponding value shows the RDS and energy barriers of catalysts. **(B)** Favorable reaction pathway from i to iv of Ag-N-C. (brown ball: C atoms, violet ball: Ag atoms, red ball: O atoms, green ball: N atoms, pink ball: H atoms).

Information), indicating a moderate interaction which is beneficial to the reversible ad/desorption in the ORR process (Lopez et al., 2005; Sun et al., 2019; Wang et al., 2021). After the adsorption, the catalytic process is divided into four elementary steps, accompanied with one electron transferring in each step(Chen et al., 2017):

$$(i)\ {}^*O_2 + H_2O\,(l) + e^- \rightarrow {}^*OOH + OH^-$$
$$(ii)\ {}^*OOH + e^- \rightarrow {}^*O + OH^-$$
$$(iii)\ {}^*O + H_2O\,(l) + e^- \rightarrow {}^*OH + OH^-$$
$$(iv)\ {}^*OH + e^- \rightarrow OH^- + {}^*$$

where the * represents the adsorption site. It is seen that the first three elementary reactions (steps i to iii) are downhill for all the catalysis, illustrating they are exothermic and spontaneous. In the last step, whereby the * OH is desorbed from the catalyst, the uphill trend on the Ag-C, Ag-gN-C and Ag-pN-C (Vacancy I) elucidates an endothermic reaction, restricting the ORR efficiency. By contrast, it remains downhill in Ag-pN-C (Vacancy II) due to the mild binding interaction between the reaction intermediates and the catalyst which enables facile desorption of OH. Therefore, the significance of pyridine nitrogen and pores in the carbon support not only facilitates a favorable uniform particle dispersion, but also guarantees a moderate binding strength for key intermediates, which improved the free energy change for the potential determining step.

4 Conclusion

In summary, we prepared a new Ag NP@N-C-900 catalyst by a one-step method, with a highly active electrocatalyst for ORR. This obtained Ag NP@N-C-900 possesses superior ORR performance with a half-wave potential of 0.83 V, a limit-current density of 7.03 mA cm^{-2}, excellent stability (≈85% activity retention after 16,000 s) and methanol resistance ability in an alkaline medium, related to well-distributed Ag nanoparticles on the ZIF-derived carbon skeleton, the high BET and high active N content. Attractively, the primary zinc–air battery based on the Ag NP@N-C-900 air-cathode offers a long cycle of 3600 min as well as excellent durability. The catalytic activity and stability exceed most of the Ag-based catalysts reported so far, and are completely comparable to commercially available Pt/C. The strategy is highlighted by its simplicity and high-yield production of a well-defined morphology, which is promising industrial merits. Meanwhile, this route can be extended to prepare other efficient electrocatalysts applied in fuel cells, supercapacitors, and batteries.

Data availability statement

The original contributions presented in the study are included in the article/Supplementary Material, further inquiries can be directed to the corresponding author.

Author contributions

Data curation, MY and JW; Formal analysis, JZ; Funding acquisition, QP; Investigation, JW and WG; Methodology, JZ, DL, and LL; Writing-review and editing, MY, YW, and JZ. All authors have read and agreed to the published version of the manuscript.

Funding

We greatly acknowledge the financial support from National Natural Science Foundation-Outstanding Youth Foundation (51971194, 51771162) and Hebei Province Talent project (A201910002), the Natural Science Foundation of Hebei Province for Innovation Groups Program (C2022203203). We would like to express our gratitude to the Ministry of Education Yangtze River scholar Professor Program (T2020124).

Conflict of interest

Author LL was employed by Chengde Iron and Steel Group Co., Ltd., HBIS Group Co., Ltd., Chengde, Hebei, China.

The remaining authors declare that the research was conducted in the absence of any commercial or financial relationships that could be construed as a potential conflict of interest.

Publisher's note

Supplementary material

The Supplementary Material for this article can be found online at: https://www.frontiersin.org/articles/10.3389/fenrg.2022.1082239/full#supplementary-material

References

Amiinu, I. S., Pu, Z., Liu, X., Owusu, K. A., Monestel, H. G. R., Boakye, F. O., et al. (2017). Multifunctional Mo-N/C@MoS_2 electrocatalysts for HER, OER, ORR, and Zn-air batteries. *Adv. Funct. Mat.* 27 (44), 1702300. doi:10.1002/adfm.201702300

Asazawa, K., Sakamoto, T., Yamaguchi, S., Yamada, K., Fujikawa, H., Tanaka, H., et al. (2009). Study of anode catalysts and fuel concentration on direct hydrazine alkaline anion-exchange membrane fuel cells. *J. Electrochem. Soc.* 156 (4), B509. doi:10.1149/1.3082129

Bai, Q., Shen, F. C., Li, S. L., Liu, J., Dong, L. Z., Wang, Z. M., et al. (2018). Cobalt@nitrogen-doped porous carbon fiber derived from the electrospun fiber of bimetal-organic framework for highly active oxygen reduction. *Small Methods* 2 (12), 1800049. doi:10.1002/smtd.201800049

Blöchl, P. E. (1994). Projector augmented-wave method. *Phys. Rev. B* 50 (24), 17953–17979. doi:10.1103/physrevb.50.17953

Cano, Z. P., Banham, D., Ye, S., Hintennach, A., Lu, J., Fowler, M., et al. (2018). Batteries and fuel cells for emerging electric vehicle markets. *Nat. Energy* 3 (4), 279–289. doi:10.1038/s41560-018-0108-1

Chala, S. A., Tsai, M. C., Su, W. N., Ibrahim, K. B., Thirumalraj, B., Chan, T. S., et al. (2020). Hierarchical 3D architectured Ag nanowires shelled with NiMn-layered double hydroxide as an efficient bifunctional oxygen electrocatalyst. *ACS Nano* 14 (2), 1770–1782. doi:10.1021/acsnano.9b07487

Chen, Y., Ji, S., Wang, Y., Dong, J., Chen, W., Li, Z., et al. (2017). Isolated single iron atoms anchored on N-doped porous carbon as an efficient electrocatalyst for the oxygen reduction reaction. *Angew. Chem. Int. Ed.* 56 (24), 6937–6941. doi:10.1002/anie.201702473

Dong, J., Sun, T., Li, S., Shan, N., Chen, J., Yan, Y., et al. (2019). 3D ordered macro-/mesoporous carbon supported Ag nanoparticles for efficient electrocatalytic oxygen reduction reaction. *J. Colloid Interface Sci.* 554, 177–182. doi:10.1016/j.jcis.2019.06.087

El-Deab, M. S., Sotomura, T., and Ohsaka, T. (2005). Oxygen reduction at electrochemically deposited crystallographically oriented Au(100)-like gold nanoparticles. *Electrochem. Commun.* 7 (1), 29–34. doi:10.1016/j.elecom.2004.10.010

Guo, F., Zhang, M., Yi, S., Li, X., Xin, R., Yang, M., et al. (2022). Metal-coordinated porous polydopamine nanospheres derived Fe_3N-FeCo encapsulated N-doped carbon as a highly efficient electrocatalyst for oxygen reduction reaction. *Nano Res. Energy* 1, e9120027.

Guo, J., Hsu, A., Chu, D., and Chen, R. (2010). Improving oxygen reduction reaction activities on carbon-supported Ag nanoparticles in alkaline solutions. *J. Phys. Chem. C* 114 (10), 4324–4330. doi:10.1021/jp910790u

Han, J., Meng, X., Lu, L., Bian, J., Li, Z., and Sun, C. (2019). Single-atom Fe-N_x-C as an efficient electrocatalyst for zinc-air batteries. *Adv. Funct. Mat.* 29, 1808872. doi:10.1002/adfm.201808872

He, W., Jiang, C., Wang, J., and Lu, L. (2014). High-rate oxygen electroreduction over graphitic-N species exposed on 3D hierarchically porous nitrogen-doped carbons. *Angew. Chem. Int. Ed.* 53 (36), 9503–9507. doi:10.1002/anie.201404333

Hu, X., Luo, G., Zhao, Q., Wu, D., Yang, T., Wen, J., et al. (2020). Ru single atoms on N-doped carbon by spatial confinement and ionic substitution strategies for high-performance Li-O_2 batteries. *J. Am. Chem. Soc.* 142 (39), 16776–16786. doi:10.1021/jacs.0c07317

Huang, M., Li, C., Zhang, L., Chen, Q., Zhen, Z., Li, Z., et al. (2018). Twin structure in $BiVO_4$ photoanodes boosting water oxidation performance through enhanced charge separation and transport. *Adv. Energy Mat.* 8 (32), 1802198. doi:10.1002/aenm.201802198

Iwase, K., Yoshioka, T., Nakanishi, S., Hashimoto, K., and Kamiya, K. (2015). Copper-modified covalent triazine frameworks as non-noble-metal electrocatalysts for oxygen reduction. *Angew. Chem. Int. Ed.* 54 (38), 11068–11072. doi:10.1002/anie.201503637

Jiang, L., Hsu, A., Chu, D., and Chen, R. (2009). Size-dependent activity of palladium nanoparticles for oxygen electroreduction in alkaline solutions. *J. Electrochem. Soc.* 156 (5), B643. doi:10.1149/1.3098478

Jiang, M., Wang, F., Yang, F., He, H., Yang, J., Zhang, W., et al. (2022). Rationalization on high-loading iron and cobalt dual metal single atoms and mechanistic insight into the oxygen reduction reaction. *Nano Energy* 93, 106793. doi:10.1016/j.nanoen.2021.106793

Kresse, G., and Furthmüller, J. (1996a). Efficiency of ab-initio total energy calculations for metals and semiconductors using a plane-wave basis set. *Comput. Mat. Sci.* 6 (1), 15–50. doi:10.1016/0927-0256(96)00008-0

Kresse, G., and Furthmüller, J. (1996b). Efficient iterative schemes for ab initio total-energy calculations using a plane-wave basis set. *Phys. Rev. B* 54 (16), 11169–11186. doi:10.1103/physrevb.54.11169

Lai, Q., Zhao, Y., Liang, Y., He, J., and Chen, J. (2016). *In situ* confinement pyrolysis transformation of ZIF-8 to nitrogen-enriched meso-microporous carbon frameworks for oxygen reduction. *Adv. Funct. Mat.* 26 (45), 8334–8344. doi:10.1002/adfm.201603607

Li, Y. J., Cui, L., Da, P. F., Qiu, K. W., Qin, W. J., Hu, W. B., et al. (2018). Multiscale structural engineering of Ni-doped CoO nanosheets for zinc-air batteries with high power density. *Adv. Mat.* 30 (46), e1804653. doi:10.1002/adma.201804653

Liu, X., Jin, R., Chen, D., Chen, L., Xing, S., Xing, H., et al. (2015). *In situ* assembly of monodispersed Ag nanoparticles in the channels of ordered mesopolymers as a highly active and reusable hydrogenation catalyst. *J. Mat. Chem. A Mat.* 3 (8), 4307–4313. doi:10.1039/c4ta06049k

Liu, Y., Wang, H., Lin, D., Zhao, J., Liu, C., Xie, J., et al. (2017). A prussian blue route to nitrogen-doped graphene aerogels as efficient electrocatalysts for oxygen reduction with enhanced active site accessibility. *Nano Res.* 10 (4), 1213–1222. doi:10.1007/s12274-016-1300-x

Lopez-Salido, I., Lim, D. C., and Kim, Y. D. (2005). Ag nanoparticles on highly ordered pyrolytic graphite (Hopg) surfaces studied using STM and XPS. *Surf. Sci.* 588 (1-3), 6–18. doi:10.1016/j.susc.2005.05.021

Pech, I. E., Gervasio, D. F., Godínez-Garcia, A., Solorza-Feria, O., and Pérez-Robles, J. F. (2015). Nanoparticles of Ag with a Pt and Pd rich surface supported on carbon as a new catalyst for the oxygen electroreduction reaction (ORR) in acid electrolytes. *J. Power Sources* 276, 365–373. doi:10.1016/j.jpowsour.2014.09.112

Ramaswamy, N., Tylus, U., Jia, Q., and Mukerjee, S. (2013). Activity descriptor identification for oxygen reduction on nonprecious electrocatalysts: Linking surface science to coordination chemistry. *J. Am. Chem. Soc.* 135 (41), 15443–15449. doi:10.1021/ja405149m

Roche, I., Chaînet, E., Chatenet, M., and Vondrák, J. (2007). Carbon-supported manganese oxide nanoparticles as electrocatalysts for the oxygen reduction reaction (ORR) in alkaline medium: Physical characterizations and ORR mechanism. *J. Phys. Chem. C* 111 (3), 1434–1443. doi:10.1021/jp0647986

Seh, Z. W., Kibsgaard, J., Dickens, C. F., Chorkendorff, I., Nørskov, J. K., and Jaramillo, T. F. (2017). Combining theory and experiment in electrocatalysis: Insights into materials design. *Science* 355 (6321), eaad4998. doi:10.1126/science.aad4998

Shen, F. C., Wang, Y., Tang, Y. J., Li, S. L., Wang, Y. R., Dong, L. Z., et al. (2017). CoV_2O_6-V_2O_5 coupled with porous N-doped reduced graphene oxide composite as a highly efficient electrocatalyst for oxygen evolution. *ACS Energy Lett.* 2 (6), 1327–1333. doi:10.1021/acsenergylett.7b00229

Su, C. Y., Cheng, H., Li, W., Liu, Z. Q., Li, N., Hou, Z., et al. (2017). Atomic modulation of FeCo-nitrogen-carbon bifunctional oxygen electrodes for rechargeable and flexible all-solid-state zinc-air battery. *Adv. Energy Mat.* 7 (13), 1602420. doi:10.1002/aenm.201602420

Sun, Y., Wang, J., Guo, J., Wang, J., and Peng, Q. (2020). Anomalous sublimation passivation of nanotwinned silver particles. *Mat. Res. Lett.* 8 (5), 195–200. doi:10.1080/21663831.2020.1739155

Sun, Y., Wang, J., Liu, Q., Xia, M., Tang, Y., Gao, F., et al. (2019). Itinerant ferromagnetic half metallic cobalt-iron couples: Promising bifunctional electrocatalysts for ORR and OER. *J. Mat. Chem. A Mat.* 7 (47), 27175–27185. doi:10.1039/c9ta08616a

Wang, J., Xu, R., Sun, Y., Liu, Q., Xia, M., Li, Y., et al. (2021). Identifying the Zn-Co binary as a robust bifunctional electrocatalyst in oxygen reduction and evolution reactions via shifting the apexes of the volcano plot. *J. Energy Chem.* 55, 162–168. doi:10.1016/j.jechem.2020.07.010

Wang, M. Q., Ye, C., Wang, M., Li, T. H., Yu, Y. N., and Bao, S. J. (2018). Synthesis of M (Fe_3C, Co, Ni)-porous carbon frameworks as high-efficient ORR catalysts. *Energy Storage Mat.* 11, 112–117. doi:10.1016/j.ensm.2017.10.003

Wu, X., Chen, F., Zhang, N., Qaseem, A., and Johnston, R. L. (2017). Engineering bimetallic Ag-Cu nanoalloys for highly efficient oxygen reduction catalysts: A guideline for designing Ag-based electrocatalysts with activity comparable to Pt/C-20%. *Small* 13 (19), 1603876. doi:10.1002/smll.201603876

Yang, J., Sun, H., Liang, H., Ji, H., Song, L., Gao, C., et al. (2016). A highly efficient metal-free oxygen reduction electrocatalyst assembled from carbon nanotubes and graphene. *Adv. Mat.* 28 (23), 4606–4613. doi:10.1002/adma.201505855

Zhang, Z., Li, H., Hu, J., Liu, B., Zhang, Q., Fernandez, C., et al. (2017). High oxygen reduction reaction activity of C-N/Ag hybrid composites for Zn-air battery. *J. Alloys Compd.* 694, 419–428. doi:10.1016/j.jallcom.2016.10.031

Zhou, R., Zheng, Y., Jaroniec, M., and Qiao, S. Z. (2016). Determination of the electron transfer number for the oxygen reduction reaction: From theory to experiment. *ACS Catal.* 6 (7), 4720–4728. doi:10.1021/acscatal.6b01581

Zhou, X., Gao, Y., Deng, S., Cheng, S., Zhang, S., Hu, H., et al. (2017). Improved oxygen reduction reaction performance of Co confined in ordered N-doped porous carbon derived from ZIF-67@PILs. *Ind. Eng. Chem. Res.* 56 (39), 11100–11110. doi:10.1021/acs.iecr.7b03417